Applied Physics Letters ARTICLE pubs.aip.org/aip/apl

Titanium oxynitride electron-selective contact for crystalline silicon solar cells

Cite as: Appl. Phys. Lett. **127**, 153901 (2025); doi: 10.1063/5.0287987
Submitted: 28 June 2025 · Accepted: 25 September 2025 ·
Published Online: 13 October 2025

View Online Export Citation CrossMark

Wenhao Li, Kun Gao, Jun Zhou, Peng Xie, Gege Yan, Xinyao Sun, and Xinbo Yang[a)]

AFFILIATIONS

College of Energy, Soochow University, Suzhou 215006, China

[a)]Author to whom correspondence should be addressed: xbyang@suda.edu.cn

ABSTRACT

Wide-bandgap metal compound-based carrier-selective contacts are being intensively developed to mitigate the carrier recombination losses at the contact regions of crystalline silicon (*c*-Si) solar cells. In this work, magnetron sputtered titanium oxynitride (TiO_xN_y) is exploited as an electron-selective contact for *c*-Si solar cells. We investigate the effect of various deposition parameters (N_2 concentration, power, and pressure) on the optoelectronic properties of TiO_xN_y films. The optimized TiO_xN_y film features a low resistivity of 9×10^{-4} Ω cm and high transmittance. The surface passivation and contact resistivity of TiO_xN_y films on c-Si were also investigated. The results demonstrate that TiO_xN_y can effectively serve as an electron-selective contact for *c*-Si solar cells due to its low WF (4.15 eV) and low contact resistivity of 9.4 mΩ cm^2 on *c*-Si. By implementing a full-area TiO_xN_y rear contact, a champion efficiency of 20.2% is obtained on the n-type *c*-Si solar cell, representing an absolute efficiency gain of 4.4%.

Crystalline silicon (*c*-Si) solar cells dominate the photovoltaic (PV) market due to their high efficiency and reliability. Currently, *c*-Si solar cells with passivating contacts have replaced the dominant role of passivated emitter and rear contact (PERC) cells.[1,2] The advanced passivating contacts based on doped silicon layers (e.g., tunnel oxide passivating contact TOPCon and silicon heterojunction technology SHJ) significantly reduce carrier recombination at both the contact and non-contact regions, thereby enhancing both the open-circuit voltage (V_{oc}) and overall power conversion efficiency (PCE).[3–5] Specifically, ultrahigh PCEs of 27.3%[6] and 26.4%[6] have been achieved on SHJ and TOPCon solar cells, respectively. Nevertheless, the high parasitic absorption of doped silicon layers impedes further PCE improvement of SHJ and TOPCon solar cells.

As a substitute, wide-bandgap metal compound-based carrier-selective contacts have gained significant attention due to the simple deposition process and minimal parasitic absorption.[7,8] Typically, metal compounds featuring a low work function (e.g., TiO_x,[9] ZnO_x,[10] TaO_x,[11] MgO_x,[12,13] Nd_2O_{3-x},[14] SrO_x,[15] SrF_x,[16] AlF_x,[17] MgF_x,[18] TiN_x,[19] TaN_x,[20] AZO,[21] MgO_x/AZO,[22] and BaO_xF_y/LiF[23]) serve as electron-selective contacts (ESCs). In contrast, high-work function materials (e.g., MoO_x,[24,25] VO_x,[26,27] WO_x,[28] NiO_x,[29] and Cu_2O[30]) can be developed as hole-selective contacts (HSCs). Up to this point, champion PCEs of 24.3%[21] and 23.8%[31] have been obtained on *c*-Si solar cells featuring electron-selective contact of SiO_2/ZnO and hole-selective contact of a-Si:H/MoO_x, respectively. By integrating the front MgO_x/AZO ESC and rear VO_x HSC,[22] a high PCE of 22.8% was achieved on *c*-Si solar cells with both-side asymmetric hetero-contacts. Although these studies have demonstrated the immense potential of these materials, the performance of c-Si solar cells remains inferior to that of silicon-based passivating contacts, primarily due to the poor surface passivation and stability. Therefore, the development of new metal compound material that simultaneously provides excellent surface passivation and low contact resistivity is crucial for further enhancing the performance of c-Si solar cells.

Recently, due to their appropriate work function and excellent conductivity, metal (oxy)nitrides have been investigated as potential ESCs for *c*-Si solar cells. For instance, TaN_x,[20] TiN_x,[19] and ZrN[32] demonstrated good electron selectivity and excellent stability, achieving moderate PCEs of 20.1%, 20.0%, and 19.7% on *c*-Si solar cells, respectively. However, it was found that high carrier concentration in metal nitrides can result in severe parasitic absorption. Yang *et al.* deposited TiO_xN_y films by ALD and developed a-Si:H/TiO_xN_y stack as an efficient ESC for *c*-Si solar cells,[33] achieving a high PCE of 22.3%. Yu *et al.* reported TiN electron-selective contact deposited by sputtering using a TiN ceramic target, achieving a much lower PCE of 18.2% on *c*-Si solar cells.[34] Compared to ALD, reactive sputtering offers a higher deposition rate and is more conducive to the flexible control of the composition of oxynitride films. In this paper, we deposited TiO_xN_y films by

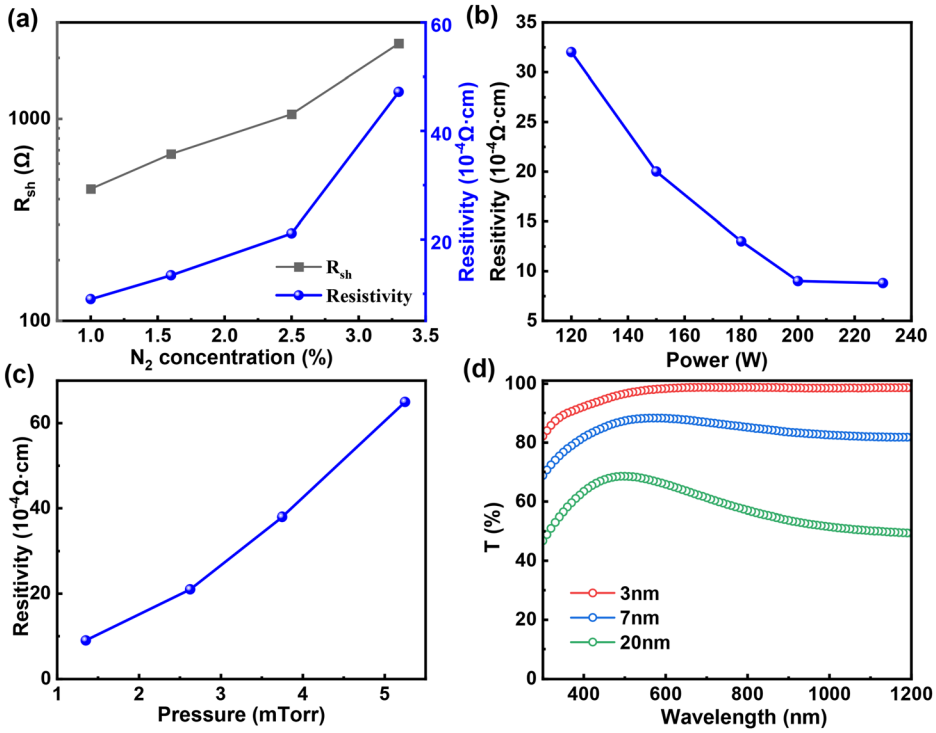

FIG. 1. (a) R_{sh} and resistivity of TiO_xN_y films (∼20 nm) as a function of nitrogen concentration. Dependence of resistivity on (b) power and (c) pressure. (d) Optical transmission spectra of TiO_xN_y films of different thicknesses.

reactive sputtering using a titanium target and optimized their optoelectronic properties. The element composition of TiO_xN_y films was analyzed, and the passivation and contact performance of TiO_xN_y on n-type *c*-Si were also investigated and optimized. Ultimately, by implementing the single-layer electron-selective TiO_xN_y contact, a PCE of 20.2% is achieved on *c*-Si.

The TiO_xN_y films were deposited using RF magnetron sputtering with varying nitrogen concentrations, powers, and chamber pressures. We first investigated the effect of nitrogen concentration on the optoelectronic properties of the films. Figure 1(a) shows the dependence of sheet resistance (R_{sh}) and the corresponding resistivity of TiO_xN_y on the nitrogen concentration. The R_{sh} rises rapidly as the nitrogen concentration increases under the same thickness (∼20 nm), and the resistivity follows a similar trend. A lowest R_{sh} of 450 Ω/sq is obtained at the lowest nitrogen concentration of 1% and this minimum value is slightly higher than that of TiN (∼250 Ω/sq) reported by Yang *et al.*[19] So the TiO_xN_y films discussed in this study were deposited under a constant nitrogen concentration of 1.0%, unless otherwise specified. Figure 1(b) illustrates the resistivity of TiO_xN_y films as a function of power. With increasing power, the resistivity of the TiO_xN_y film decreases continuously, which can be attributed to the improved film density under high plasma energy. As the power increases from 120 to 200 W, the resistivity significantly decreases from 3.3×10^{-3} to 9×10^{-4} Ω cm. Further increasing the power to 230 W results in a slight decrease in resistivity to 8.8×10^{-4} Ω cm. In contrast, as shown in Fig. 1(c), the effect of chamber pressure exhibits an opposite trend: as the pressure increases, the resistivity increases significantly. Therefore, high power (200 W) and low pressure (1.35 mTorr) are more favorable for depositing TiO_xN_y films with high conductivity. Additionally, we compared the optical transmission spectra of TiO_xN_y films with varying thicknesses. As shown in Fig. 1(d), the transmittance of TiO_xN_y films decreases dramatically with increasing thickness. At a thickness of 3 nm, the TiO_xN_y film shows an average transmittance of 97.7%, whereas it decreases to 60.6% for 20 nm. The reduction in long-wavelength transmittance with increasing TiO_xN_y film thickness is probably ascribed to the free carrier absorption due to its quasi-metallic property and high carrier density for thick TiO_xN_y film.

High-resolution x-ray photoelectron spectroscopy (XPS) was employed to determine the chemical composition of TiO_xN_y films. Figure 2(a) displays the XPS core-level spectrum of Ti 2p in the film, which can be deconvoluted into three doublets between Ti $2p_{3/2}$ and Ti $2p_{1/2}$. The Ti $2p_{3/2}$ peak located at 455.1 eV and the $2p_{1/2}$ peak located at 461.1 eV correspond to the Ti–N bond, the $2p_{3/2}$ peak located at 456.7 eV and the 2p1/2 peak located at 463.1 eV correspond to the Ti–ON bond, and the $2p_{3/2}$ peak located at 458.3 eV and the

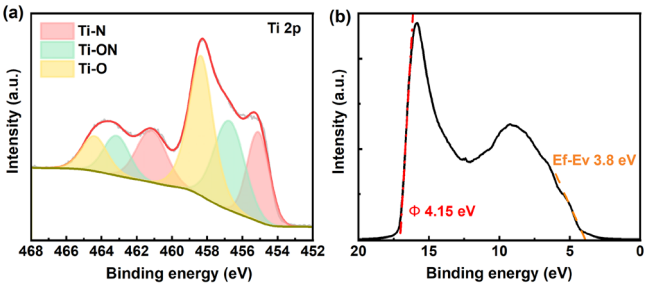

FIG. 2. (a) XPS core-level spectrum of Ti 2p and (b) UPS spectrum for TiO_xN_y films.

$2p_{1/2}$ peak located at 464.4 eV correspond to the Ti–O bond.[34,35] The calculated percentages of TiN_x, TiO_xN_y, and TiO_x are 23.6%, 32.7%, and 43.7%, respectively, so we define the film with a non-stoichiometric chemical formula TiO_xN_y. The residual oxygen in the chamber during the deposition process results in the formation of TiO_xN_y and TiO_x. The optical bandgap of TiO_xN_y was determined to be approximately 3.42 eV, obtained via ultraviolet-visible (UV-vis) spectroscopy using T_{auc} plots (Fig. S1), which is higher than that of 3.2 eV of TiN_x.[19] The incorporation of oxygen achieves a balance between the properties of high transparency of TiO_2[9] and high conductivity of TiN_x.[19] Therefore, controlling the oxygen concentration during the deposition process is also crucial. As shown in Fig. 2(b), the work function, calculated from the onset of the ultraviolet photoelectron spectroscopy (UPS) spectrum, is determined to be 4.15 eV. The E_f-E_v value (3.8 eV) is obtained from the cutoff in the UPS spectrum, indicating that the Fermi level is close to the conduction band, which is characteristic of n-type semiconductors.

The contact resistivity (ρ_c) of the n-Si/TiO_xN_y/Al heterocontacts was measured using the transfer-length method (TLM),[36] as shown in Fig. 3(a). By measuring the resistance at different electrode spacings and fitting the linear relationship between resistance and spacing, the ρ_c of the heterocontact can be extracted. Figure 3(b) shows the dark J–V curves of Al/Si Schottky structures, with and without TiO_xN_y interlayer on the different c-Si substrates. The direct n-Si/Al contact exhibits typical Schottky behavior (blue line), which can be attributed to the presence of a large Schottky barrier at the interface, hindering the flow of electrons from the n-Si. The insertion of the TiO_xN_y interlayer alleviates the Schottky behavior, resulting in Ohmic contact characteristics in the J–V curve (red line). In contrast, the opposite effect is observed on the p-Si substrate. The results indicate that the TiO_xN_y/Si heterojunction can effectively reduce the Schottky barrier height of n-Si/Al and block holes effectively. Figure 3(c) shows the dark J–V curves under different spacings, a lowest ρ_c of 9.4 mΩ cm^2 is extracted with 3 nm TiO_xN_y. The ρ_c outperforms that of other reported electron-selective contacts, including sputtered TiN_x[19] (16.4 mΩ cm^2) and ALD TaN_x[20] ($\sim$42 mΩ cm^2). Figure 3(d) displays the effect of TiO_xN_y thickness on the ρ_c of n-Si/TiO_xN_y/Al heterocontacts. The ρ_c increases from 9.4 to 113 mΩ cm^2 as the thickness increases from 3 to 8 nm, which can be ascribed to enhanced tunneling resistance due to increased bulk resistance.

Passivation quality is another critical parameter for high-quality passivating contacts, and the implied open-circuit voltage (iV_{oc}) measured by the Sinton Lifetime Tester can effectively reflect this performance. Figures S2(a) and S2(c) illustrate the iV_{oc} and effective minority carrier lifetimes (τ_{eff}) of n-Si passivated by single-layer TiO_xN_y (3–8 nm) as a function of annealing temperature. As the annealing temperature increases from 200 to 600 °C, the iV_{oc} of TiO_xN_y passivated n-Si fluctuates around 540 mV and the τ_{eff} of TiO_xN_y passivated n-Si fluctuates around 2 μs, indicating a lower passivation level. This demonstrates that the single-layer TiO_xN_y thin films cannot offer effective passivation. The thermally grown SiO_x layer was proven to be effective in promoting surface passivation for ZnO[21] and TiO_2[9] passivating contacts, and we tried to implement the tunnel SiO_2 (0.7 nm) into the TiO_xN_y contact as well. Unfortunately, we found that SiO_x passivation interlayer cannot improve the passivation quality of TiO_xN_y contact, neither before annealing nor after annealing, as shown in Figs. S2(b) and S2(d). The poor passivation quality might be attributed to sputtering damage on the c-Si substrate, which induces surface defects that cannot be cured by annealing.

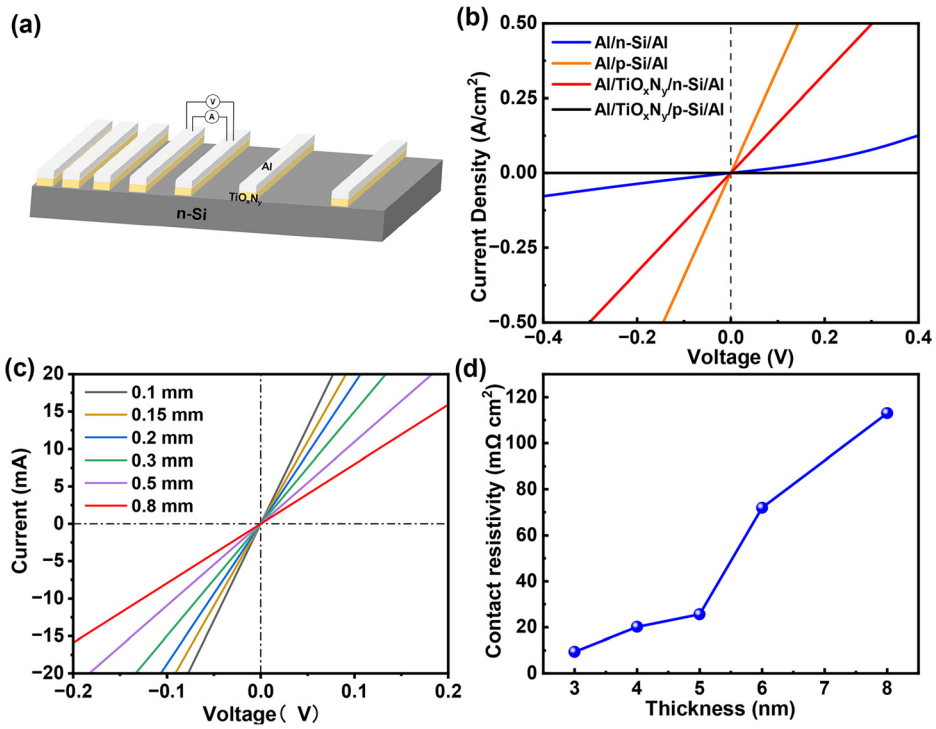

FIG. 3. (a) Schematic of the TLM structure. (b) Dark J–V curves of Al/Si Schottky structures with and without a TiO_xN_y interlayer (3 nm). (c) Dark J–V curves of n-Si/TiO_xN_y/Al heterocontact under different spacings. (d) Dependence of ρ_c on the TiO_xN_y film thickness of n-Si/TiO_xN_y/Al heterocontacts.

To verify its electron-selective contact performance, we designed and fabricated n-Si solar cells with full-area TiO_xN_y rear contacts, as shown in Fig. 4(a). The cell features a boron diffused p^+ emitter on textured random pyramids that are passivated by Al_2O_3/SiN_x stack on the front side and a rear full-area TiO_xN_y electron-selective contact (3 nm) capped with thermally evaporated Al electrodes. Figure 4(b) shows the J–V curves of the n-Si solar cells with and without TiO_xN_y. The control device with a simple Al rear contact exhibits a low V_{oc} of 555 mV and a fill factor (FF) of 75.1%, resulting in a low PCE of 15.8%, which can be ascribed to the high carrier recombination and high contact resistance at the rear side. The device performance was significantly improved after the insertion of a 3 nm TiO_xN_y interlayer, owing to the reduced carrier recombination and decreased contact resistivity. The champion device achieved a PCE of 20.2% (V_{oc} 619 mV, J_{sc} 39.4 mA/cm^2, and FF 82.9%), which is higher than that of ALD TaN_x,[20] sputtered TiNx,[19] and sputtered ZrN[32] contacts. The PCE is mainly limited by a relatively low V_{oc}, which is consistent with the poor surface passivation of TiO_xN_y.

Figure 4(c) displays the external quantum efficiency (EQE) spectra of the devices with and without a TiO_xN_y interlayer. Both cells show the same front structure, displaying minimal variation in the EQE in the short-wavelength range (<800 nm). However, in the long-wavelength range (>800 nm), the EQE is significantly improved after the introduction of a thin TiO_xN_y interlayer, confirming that the n-Si/TiO_xN_y heterojunction can effectively reduce carrier recombination at the rear side. Although the improved EQE suggests an increase in the effective minority carrier diffusion length, the corresponding enhancement in V_{oc} does not result solely from an extended carrier lifetime. Instead, it arises from the mitigation of metal-induced gap states on c-Si and the subsequent de-pinning of the Fermi level.[37] The calculated J_{sc} for the champion device, obtained by integrating the product of EQE and AM1.5 spectrum and correcting for the approximate contact fraction, is shown to be 39.3 mA/cm^2, which is in good agreement with the measured J_{sc} value. We re-introduced the SiO_x passivation layer to investigate its impact on device performance. Unfortunately, the device performance decreases, resulting from slightly reduced V_{oc} and FF, as shown in Fig. S3. The growth method and thickness of the SiO_x layer are crucial for its quality and can significantly impact the passivating contact. Therefore, further optimizing the SiO_x deposition process is key to utilizing it as a passivation layer in future applications. Figures 4(d) and S4 show the statistical distribution of photovoltaic parameters of seven devices with TiO_xN_y contacts and three control devices, evaluating the reliability of n-Si cells with TiO_xN_y contacts.

Finally, we investigate the environmental and thermal stability of the c-Si solar cells with TiO_xN_y contact. Figure 5(a) shows the photovoltaic parameters of the best n-Si cell with TiO_xN_y contact after being stored in air for 40 days (25–30 °C, 40%–50% humidity). A slight decrease in the PCE (−3.6% relatively) can be observed, due to the increased ρ_c of n-Si/TiO_xN_y/Al (Fig. S5), probably ascribed to the undesirable interface reaction between TiO_xN_y and Al, along with the oxidation of the Ag electrode for the unencapsulated devices, both of which increase the series resistance. Figure 5(b) displays the thermal stability of the device, featuring a negligible PCE degradation up to 400 °C. With further increases to 500 °C, the PCE reduces significantly. Figure S6 shows the change in V_{oc}, FF, and J_{sc} of the best device as a function of the forming gas annealing at different temperatures for 15 min. The V_{oc} reduction might be attributed to the degradation of the front Al_2O_3/SiN_x passivation, which was believed to be stable up to

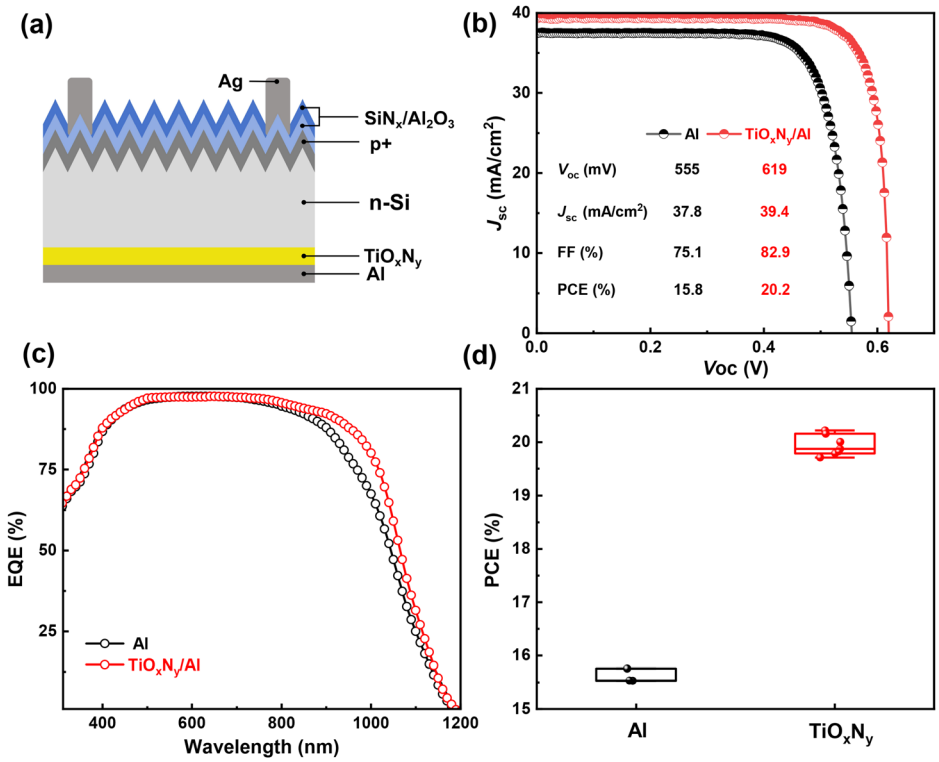

FIG. 4. (a) A schematic illustration of the n-Si solar cell with full-area TiO_xN_y contact. (b) Light J–V curves and photovoltaic parameters. (c) EQE of the cells with and without TiO_xN_y contact. (d) Statistical distribution of the PCE for n-Si cells with different rear contacts, including three control cells with Al contact and seven cells with TiO_xN_y contacts.

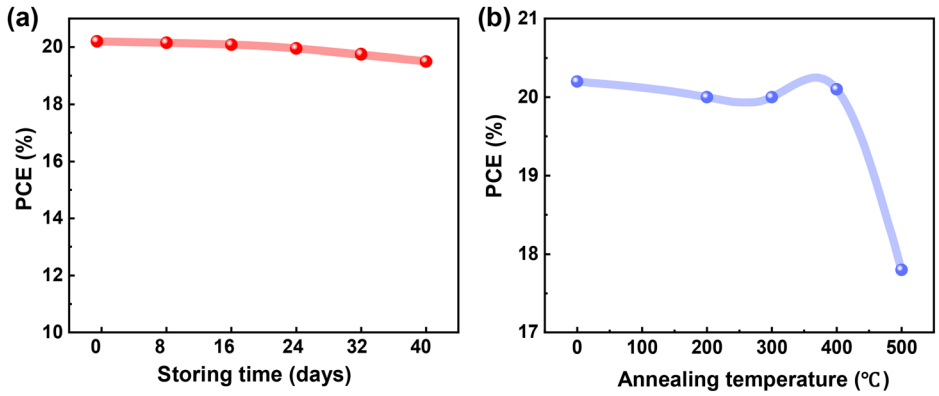

FIG. 5. (a) The environmental stability in air of *c*-Si solar cells with TiO_xN_y electron-selective contact. (b) The thermal stability of *c*-Si solar cells with TiO_xN_y electron-selective contact.

425 °C.[38] The FF degradation might be ascribed to the increased contact resistivity at the rear TiO_xN_y contact, which probably reacts with the Al electrode. Therefore, the device degradation stems from the deterioration of both the front and rear contacts under high temperatures.

In conclusion, we have developed TiO_xN_y electron-selective contacts for *c*-Si solar cells utilizing magnetron sputtering. The optoelectronic performance and elemental composition of TiO_xN_y films, as well as their contact properties on *n*-Si and device performance, are investigated and optimized. The TiO_xN_y films exhibit a low WF of 4.15 eV and a wide bandgap of 3.42 eV. The *n*-Si/TiO_xN_y/Al heterocontact demonstrated hole-blocking behavior, with a very low contact resistivity of 9.4 mΩ cm^2. The TiO_xN_y contact was integrated into the c-Si solar cell, achieving an improved efficiency of 20.2%. The insufficient surface passivation limits the device efficiency; thus, further improvement is necessary. This work broadens the application of transition-metal oxynitride passivating contact for *c*-Si solar cells.

See the supplementary material for additional data on specific experimental section and data.

The authors acknowledge the financial support from the National Natural Science Foundation of China (No. 62174114), the National Key R&D Program of China (No. 2022YFB4200203), and the Department of Science and Technology of Jiangsu Province (Nos. BE2022027, BE2022036, and BE2022023).

AUTHOR DECLARATIONS

Conflict of Interest

The authors have no conflicts to disclose.

Author Contributions

Wenhao Li: Data curation (equal); Formal analysis (equal); Visualization (equal); Writing – original draft (lead); Writing – review & editing (equal). **Kun Gao:** Formal analysis (equal); Methodology (equal); Writing – review & editing (equal). **Jun Zhou:** Writing – review & editing (equal). **Peng Xie:** Writing – review & editing (equal). **Gege Yan:** Writing – review & editing (equal). **Xinyao Sun:** Writing – review & editing (equal). **Xinbo Yang**: Conceptualization (equal); Funding acquisition (equal); Resources (equal); Supervision (equal); Writing – review & editing (equal).

DATA AVAILABILITY

The data that support the findings of this study are available from the corresponding author upon reasonable request.

REFERENCES

[1] M. Hermle, F. Feldmann, M. Bivour, J. C. Goldschmidt, and S. W. Glunz, Appl. Phys. Rev. **7**(2), 021305 (2020).
[2] T. G. Allen, J. Bullock, X. Yang, A. Javey, and S. De Wolf, Nat. Energy **4**, 914–928 (2019).
[3] Y. Liu, Y. Li, Y. Wu, G. Yang, L. Mazzarella, P. Procel-Moya, A. C. Tamboli, K. Weber, M. Boccard, O. Isabella, X. Yang, and B. Sun, Mater. Sci. Eng.: R: Rep. **142**, 100579 (2020).
[4] M. Tanaka, M. Taguchi, T. Matsuyama, T. Sawada, S. Tsuda, S. Nakano, H. Hanafusa, and Y. Kuwano, Jpn. J. Appl. Phys., Part 1 **31**, 3518–3522 (1992).
[5] F. Feldmann, M. Bivour, C. Reichel, M. Hermle, and S. W. Glunz, Sol. Energy Mater. Sol. Cells **120**, 270–274 (2014).
[6] M. A. Green, E. D. Dunlop, M. Yoshita, N. Kopidakis, K. Bothe, G. Siefer, X. Hao, and J. Y. Jiang, Prog. Photovoltaics Res. Appl. **33**(1), 3–15 (2024).
[7] J. Melskens, B. W. H. van de Loo, B. Macco, L. E. Black, S. Smit, and W. M. M. Kessels, IEEE J. Photovoltaics **8**(2), 373–388 (2018).
[8] K. Gao, Q. Bi, X. Wang, W. Liu, C. Xing, K. Li, D. Xu, Z. Su, C. Zhang, J. Yu, D. Li, B. Sun, J. Bullock, X. Zhang, and X. Yang, Adv. Mater. **34**(26), 2200344 (2022).
[9] X. Yang, Q. Bi, H. Ali, K. Davis, W. V. Schoenfeld, and K. Weber, Adv. Mater. **28**(28), 5891–5897 (2016).
[10] F. Wang, S. Zhao, B. Liu, Y. Li, Q. Ren, R. Du, N. Wang, C. Wei, X. Chen, G. Wang, B. Yan, Y. Zhao, and X. Zhang, Nano Energy **39**, 437–443 (2017).
[11] Y. Wan, S. K. Karuturi, C. Samundsett, J. Bullock, M. Hettick, D. Yan, J. Peng, P. R. Narangari, S. Mokkapati, H. H. Tan, C. Jagadish, A. Javey, and A. Cuevas, ACS Energy Lett. **3**(1), 125–131 (2018).
[12] K. Li, K. Gao, X. Wang, X. Lou, D. Xu, C. Xing, W. Li, H. Li, and X. Yang, Sci. China Mater. **67**, 2866–2872 (2024).
[13] Y. Wan, C. Samundsett, J. Bullock, M. Hettick, T. Allen, D. Yan, J. Peng, Y. Wu, J. Cui, A. Javey, and A. Cuevas, Adv. Energy Mater. **7**(5), 1601863 (2017).
[14] K. Gao, W. Li, X. Chen, P. Xie, J. Zhou, C. Yu, J. Mao, P. Zheng, X. Zhang, and X. Yang, Sol. Energy Mater. Sol. Cells **282**, 113363 (2025).
[15] C. Xing, W. Gu, K. Gao, B. Shao, C. Jiang, G. Bai, D. Xu, W. Xing, K. Li, Z. Song, Z. Su, J. Mao, X. Zhang, P. Zheng, W. Zhang, X. Zhang, Y. Wang, X. Yang, and B. Sun, Sol. RRL **7**(9), 2201100 (2023).
[16] C. Xing, C. Jiang, W. Gu, W. Lou, K. Gao, Y. Song, B. Shao, K. Li, X. Wang, D. Xu, X. Zhang, Y. Wang, X. Yang, and B. Sun, Prog. Photovoltaics Res. Appl. **32**(1), 35–44 (2024).
[17] K. Gao, C. Xing, D. Xu, X. Lou, X. Wang, K. Li, W. Li, J. Mao, P. Zheng, X. Zhang, and X. Yang, Small **20**(29), 2310352 (2024).
[18] Y. Wan, C. Samundsett, J. Bullock, T. Allen, M. Hettick, D. Yan, P. Zheng, X. Zhang, J. Cui, J. McKeon, A. Javey, and A. Cuevas, ACS Appl. Mater. Interfaces **8**(23), 14671–14677 (2016).

[19]X. Yang, W. Liu, M. D. Bastiani, T. Allen, J. Kang, H. Xu, E. Aydin, L. Xu, Q. Bi, H. Dang, E. Alhabshi, K. Kotsovos, A. Alsaggaf, I. Gereige, Y. Wan, J. Peng, C. Samundsett, A. Cuevas, and S. De Wolf, Joule **3**(5), 1314–1327 (2019).
[20]X. Yang, E. Aydin, H. Xu, J. Kang, M. Hedhili, W. Liu, Y. Wan, J. Peng, C. Samundsett, A. Cuevas, and S. De Wolf, Adv. Energy Mater. **8**(20), 1800608 (2018).
[21]K. Gao, D. Xu, J. Wang, Q. Bi, Z. Wu, H. Lin, S. Wang, W. Shi, C. Yu, F. Cao, Y. Diao, J. Xie, X. Wang, K. Li, X. Lou, W. Li, C. Xing, Y. Wang, T. Yan, D. Zhang, S. De Wolf, X. Zhang, and X. Yang, Adv. Funct. Mater. **35**(4), 2415039 (2025).
[22]D. Xu, Q. Bi, K. Li, K. Gao, X. Wang, W. Shi, S. Wang, C. Xing, X. Zhang, and X. Yang, Adv. Funct. Mater. **34**(44), 2407290 (2024).
[23]C. Xing, W. Gu, Z. Xiang, X. Lou, X. Wang, X. Zhang, Y. Wang, X. Yang, and B. Sun, Chem. Eng. J. **481**, 148568 (2024).
[24]J. Dréon, Q. Jeangros, J. Cattin, J. Haschke, L. Antognini, C. Ballif, and M. Boccard, Nano Energy **70**, 104495 (2020).
[25]J. Li, T. Pan, J. Wang, S. Cao, Y. Lin, B. Hoex, Z. Ma, L. Lu, L. Yang, B. Sun, and D. Li, ACS Appl. Mater. Interfaces **12**(32), 36778–36786 (2020).
[26]G. Du, L. Li, X. Yang, X. Zhou, Z. Su, P. Cheng, Y. Lin, L. Lu, J. Wang, L. Yang, X. Gao, X. Chen, and D. Li, Adv. Mater. Interfaces **8**(22), 2100989 (2021).
[27]X. Yang, H. Xu, W. Liu, Q. Bi, L. Xu, J. Kang, M. N. Hedhili, B. Sun, X. Zhang, and S. De Wolf, Adv. Electron. Mater. **6**(8), 2000467 (2020).
[28]M. Bivour, J. Temmler, H. Steinkemper, and M. Hermle, Sol. Energy Mater. Sol. Cells **142**, 34–41 (2015).
[29]G. Du, L. Li, H. Zhu, L. Lu, X. Zhou, Z. Gu, S. Zhang, X. Yang, J. Wang, L. Yang, X. Chen, and D. Li, EcoMat **4**(3), e12175 (2022).
[30]L. Li, L. Ying, Y. Lin, X. Li, X. Zhou, G. Du, Y. Gao, W. Liu, L. Lu, J. Wang, L. Yang, S. Zhang, and D. Li, Adv. Funct. Mater. **32**(43), 2207158 (2022).
[31]L. Cao, P. Procel, A. Alcañiz, J. Yan, F. Tichelaar, E. Özkol, Y. Zhao, C. Han, G. Yang, Z. Yao, M. Zeman, R. Santbergen, L. Mazzarella, and O. Isabella, Prog. Photovoltaics Res. Appl. **31**(12), 1245–1254 (2023).
[32]J. Tian, K. Xu, G. Wang, H. Jiang, Y. Liu, P. Zhu, and D. Wang, Appl. Phys. Lett. **122**(11), 113903 (2023).
[33]X. Yang, Y. Lin, J. Liu, W. Liu, Q. Bi, X. Song, J. Kang, F. Xu, L. Xu, M. N. Hedhili, D. Baran, X. Zhang, T. D. Anthopoulos, and S. D. Wolf, Adv. Mater. **32**(32), 2002608 (2020).
[34]J. Yu, Y. Chen, J. He, Y. Bai, R. Su, T. Cao, W. Liu, and T. Chen, Sol. Energy Mater. Sol. Cells **260**, 112491 (2023).
[35]M. Kot, K. Henkel, C. Das, S. Brizzi, I. Kärkkänen, J. Schneidewind, F. Naumann, H. Gargouri, and D. Schmeißer, Surf. Coat. Technol. **324**, 586–593 (2017).
[36]G. K. Reeves and H. B. Harrison, IEEE Electron Device Lett. **3**(5), 111–113 (1982).
[37]Z. Xin, Y. Ding, Y. Zhu, C. Fu, Z. Yao, Q. Chen, G. Liu, and F. Shan, Adv. Electron. Mater. **6**, 1901110 (2020).
[38]J. Schmidt, B. Veith, and R. Brendel, Phys. Status Solidi RRL **3**(9), 287–289 (2009).